Available online at www.sciencedirect.com
SCIENCE DIRECT®
International Journal of Heat and Mass Transfer 48 (2005) 1128–1136
International Journal of HEAT and MASS TRANSFER
www.elsevier.com/locate/ijhmt

Solution of transport equations on unstructured meshes with cell-centered colocated variables. Part II: Applications

S. Pimpalnerkar, M. Kulkarni, A.W. Date *

Mechanical Engineering Department, Indian Institute of Technology, Bombay, Powai, Mumbai 400 076, India

Received 2 April 2004; received in revised form 9 September 2004
Available online 8 December 2004

Abstract

This paper describes applications of the discretization procedure presented in the companion paper [A.W. Date, Solution of transport equations on unstructured meshes with cell-centered colocated variables. Part I. Discretization, Companion Paper, this volume]. Six problems having different domain complexities, presence of body and surface forces and, boundary conditions are solved. Where possible, the solutions are compared with published experimental or numerical data.

Keywords: SIMPLE algorithm; Unstructured meshes; Cubic cavity; T-branch; Twisted tape; Nozzle

1. Introduction

The discretization procedure described in Part I of this paper has employed novel *line-structure*. It is of interest, therefore, to demonstrate the predictive capability of this procedure. For this purpose, six problems are considered:

1. Flow in a lid-driven cubic cavity.
2. Buoyancy-driven flow and heat transfer in a tilted cubic-cavity.
3. Flow in a 2D planar T-branch.
4. Flow in a 3D branched channel of square cross-section.
5. Flow and heat transfer in a tube containing a twisted tape.
6. Flow in a subsonic-to-supersonic convergent-divergent nozzle.

The present solutions, where applicable, are compared with previously published experimental or numerical results. Details of mesh-size, relaxation parameters and convergence are given. All computations are performed using Pentium-II (400 MHz) personal computer.

2. Presentation of results

2.1. Lid-driven cubic cavity

Fig. 1a shows the lid-driven cubic cavity. In this case, the mesh with hexahedral cells is employed. Computations are performed with different number of uniformly

* Corresponding author. Tel.: +91 22 25767517; fax: +91 2225726875.
E-mail address: awdate@me.iitb.ac.in (A.W. Date).

0017-9310/$ - see front matter © 2004 Elsevier Ltd. All rights reserved.
doi:10.1016/j.ijheatmasstransfer.2004.09.037

Nomenclature

D	channel dimension
f	fanning friction factor
M	Mach number
p	pressure
Nu	Nusselt number
Pr	Prandtl number
Ra	Rayleigh number
Re	Reynolds number
T	temperature

Greek symbols

α	under-relaxation factor for velocity
β	under-relaxation factor for pressure or blending factor
μ	dynamic viscosity
ρ	density
Φ	general variable

spaced vertices ($12^3, 16^3, 22^3$). The maximum momentum and mass residuals are reduced to less than 10^{-5}. All computations are performed for $Re = U_{lid}L/\nu = 400$ where L is the length of cavity sides.

Fig. 2 shows the effect of blending parameter β used in the convection scheme [1] on the predicted u/U_{lid}. The results (at $X = Z = 0.5$) are plotted for 12^3 mesh. It is seen that the predicted peak negative velocity increases with β. Similar tendencies were observed with finer meshes. Hence, all results plotted in Fig. 3 are obtained using CDS ($\beta = 1$) and are shown by open symbols. For reference, computed mid-cavity profile using 51^3 structured-cartesian grids and UDS is also plotted (solid line). It is seen that the maximum negative velocity ($u/U_{lid} = -0.198$) predicted with 9261 elements and CDS exceeds that predicted by much finer structured grid UDS predictions. Thus, numerical diffusion introduced by UDS appears to be significant. In fact, the present unstructured mesh predictions with 9261 elements and CDS compare extremely favourably with those predicted (not shown) by Jiang et al. [2] using finite element method and by Zhao and Zhang [3] who employ third order accurate upwind scheme with 455,625 tetrahedral elements.

2.2. Buoyancy-driven flow in a tilted cavity

Fig. 1b shows the tilted cavity in which the face at $x/L = 0$ is hot and that at $x/L = 1$ is cold. All other side walls are perfectly conducting so that the temperature distributions on these walls are given by $T = T_h - (T_h - T_c)x/L$. Leong et al. [4,5] have presented experimental data for different Rayleigh numbers (Ra) using air ($Pr = 0.7$) as the working medium. At CHT'01 conference, the data were predicted by several researchers using in-house and commercially available computer codes [6] for three tilt angles $\Phi = 0°$, 45° and 90°. The objective here is to repeat these computations using

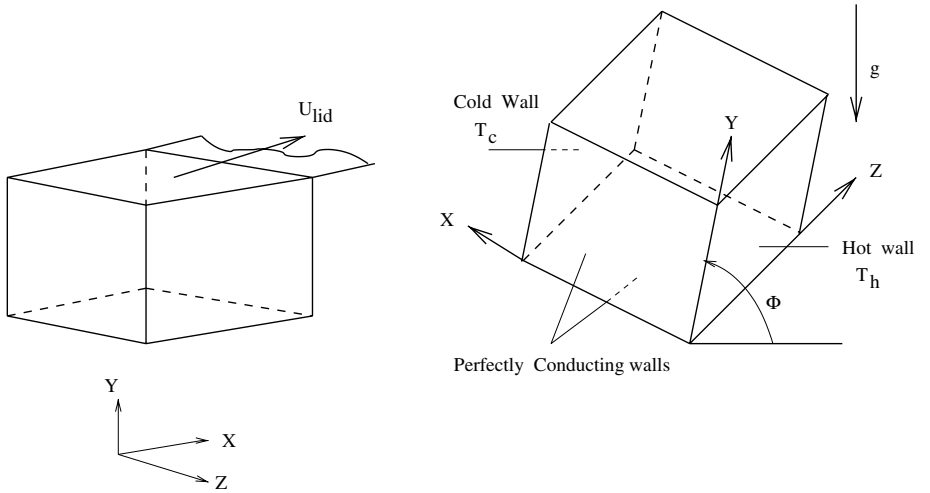

(a) Lid-Driven Cubic Cavity (b) Tilted Cubic Cavity

Fig. 1. Cubic cavity.

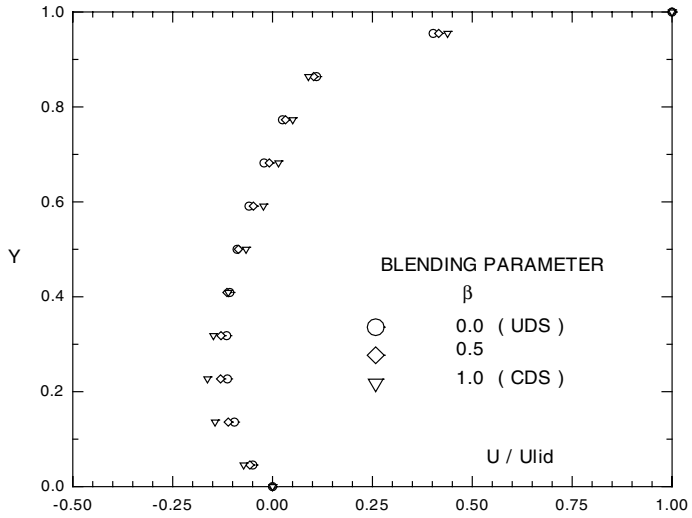

Fig. 2. Effect of β-1131 elements—lid-driven cavity.

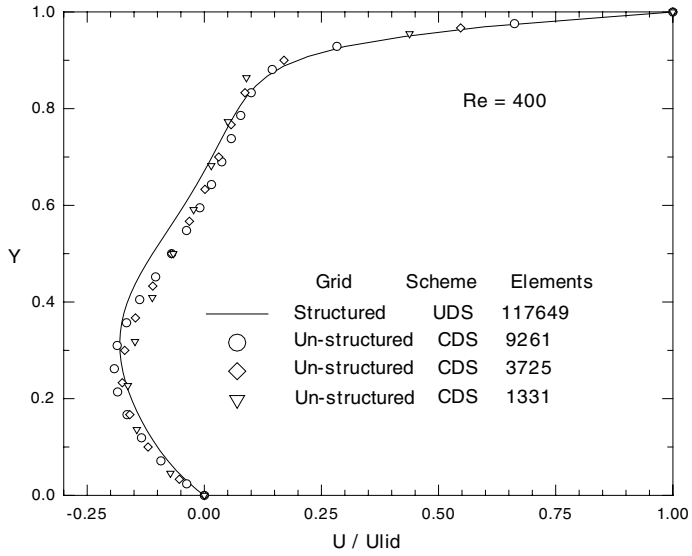

Fig. 3. Effect of mesh size—lid-driven cavity.

the present discretization procedure and carry out similar comparisons.

For the purpose of computations, non-uniform hexahedral elements were used. [1] Uniform properties were assumed ($\rho = C_p = 1$, $\mu = 0.01$). The x- and y-momentum equations were sensitised to buoyancy force term accounting for effect of angle Φ. The average wall heat transfers at hot and cold walls were expressed through Nusselt numbers

$$Nu_{\mathrm{h,c}} = \frac{\int_0^L \int_0^L \partial T/\partial x|_{\mathrm{h,c}}\, \mathrm{d}y\, \mathrm{d}z}{(T_{\mathrm{h}} - T_{\mathrm{c}})} \tag{1}$$

Table 1 shows the comparisons. Only those authors who predicted for all specified Ra at CHT01 conference are mentioned in the table. The number of elements used by different authors were: 64,000 (hex) [7], 256,000 (hex)

[1] The coordinates of vertices were $x, y = 0.0, 0.01, 0.03, 0.06, 0.1, 0.2, 0.3, 0.4, 0.5, 0.6, 0.7, 0.8, 0.9, 0.94, 0.97, 0.99, 1.0$ and $z = 0.0, 0.01, 0.03, 0.06, 0.1, 0.2, 0.3, 0.4, 0.5$ Thus, $z = 0.5$ was treated as plane of symmetry.

Table 1
Nusselt numbers for tilted cubic cavity

Ψ	Ra	Expt [4]	In-house [7]	FLUENT [10]	FLUENT [8]	CFX [9]	Present
90	10^5	3.069–3.125	3.11	3.195	3.09	3.10	3.136
	10^6	6.313–6.453	6.53	6.25	7.26	6.43	6.476
	10^7	12.82–13.14	13.05	13.84	16.76	13.10	12.85
	10^8	26.36–27.04	24.86	28.34	38.20	24.99	28.01
45	10^5	3.458–3.526	3.575	3.509	3.44	3.51	3.528
	10^6	8.736–8.938	8.80	9.285	8.58	8.61	8.991
	10^7	17.29–17.71	17.10	18.45	17.03	15.85	18.11
0	10^5	3.474–3.544	3.24	3.75	3.40	3.30	3.17
	10^6	7.792–7.974	8.12	8.33	7.38	7.57	7.85
	10^7	15.19–15.57	14.78	–	15.44	14.14	16.25

[10], 32,000 (hex) [9] and 294,173 (tet) [8]. In contrast, the present predictions are obtained with 2048 hexahedral elements and CDS.

It was found that while at low values of Ra, steady-state calculations with constant under-relaxation factor α for all variables were adequate for obtaining converged solutions, at higher values of Ra, unsteady calculations were necessary. For such calculations, the temperature profile at $t = 0$ was taken to be linear in x-direction. Nusselt numbers obtained by unsteady calculations showed oscillations with time. A typical oscillatory behaviour for $\Phi = 0$ and $Ra = 10^6$ is shown in Fig. 4. In such cases, the hot-wall and cold-wall Nusselt numbers were also not equal at every instant of time. As such, the Nu values were averaged over last few hundred steps at hot wall and are therefore underlined in Table 1. While this introduces ambiguity, it none-the-less is the practice adopted by other investigators mentioned above.

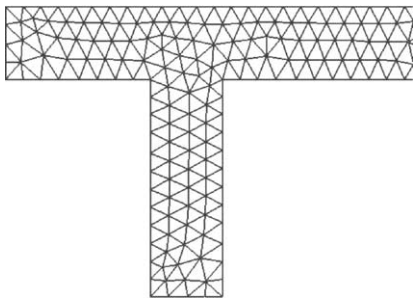

Fig. 5. Unstructured mesh—2D T-branch.

Table 1 shows that the presently predicted Nu values are in good agreement with experimental values for $\Phi = 90°$ inspite of the relatively small number of elements used in the computations. For lower angles and high values of Ra, the disagreements are moderate

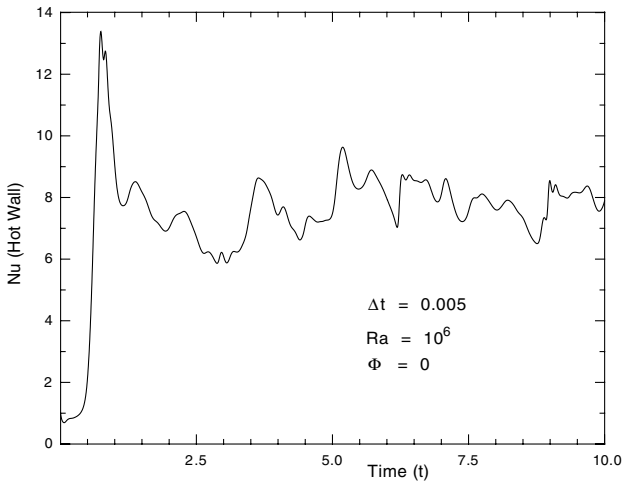

Fig. 4. Time variation of Nu_h.

indicating that further mesh-refinement will bring closer agreements.

2.3. Flow in a 2D planar T-branch

Fig. 5 considers laminar flow a 2D-plane channel having a T-branch. Flow (fully-developed velocity profile) enters the main branch from the left and is divided into T-branch and the main branch. The widths (D) of the main and T-branch are identical. The length of the main branch is 6D and that of the T-branch is 3D. The pressure at the two exit planes is fixed ($p_{ex} = 1$). The objective is to determine the fraction of inflow leaving the main branch.

In the present computations, the problem is solved using triangular *coarse* mesh with 299 elements (191 vertices). The elements were generated using ANSYS. The predicted flow-fractions are compared with predictions of Hayes et al. [17] in Fig. 6. The figure shows that inspite of mesh-coarseness, the predicted flow fractions agree with previous predictions with maximum deviation of 7%. The computations were repeated with 4761 elements. Now, the results are found to be good (except at the lowest Reynolds number). This problem has been computed by [11] with 2721 adaptive quadrilateral meshes within the cell-centred approach and with 8100 quadrilateral meshes within the vertex-centred approach by [16].

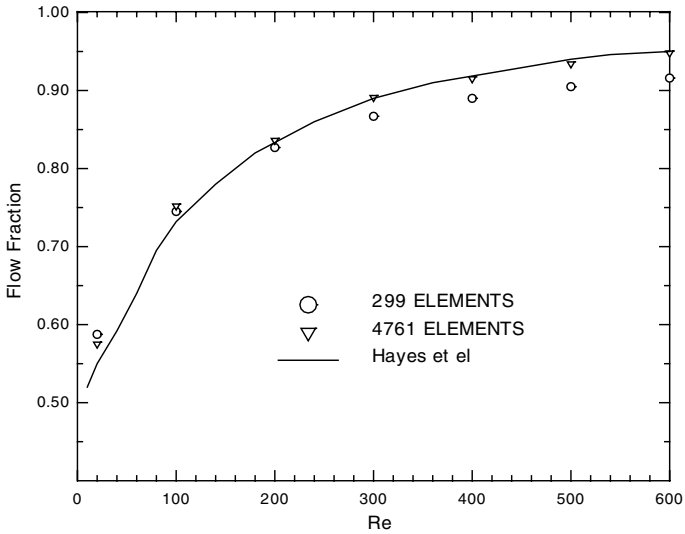

Fig. 6. Variation of flow fraction with Re—2D T-branch.

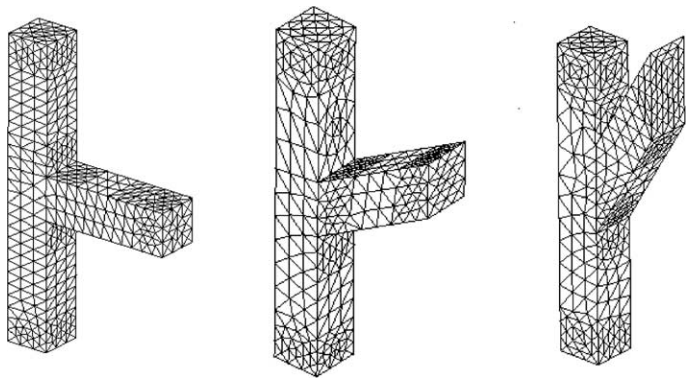

Fig. 7. Unstructured mesh—3D branch $\Psi = 90°, 60°, 30°$.

2.4. Flow in a 3D branched channel

Consider laminar flow in a branched channel (see Fig. 7) of square cross-section (each side D). The flow enters the main branch from the bottom with fully-developed velocity profile given by [21]

$$v = 2.1157 \times \left\{1 - \left(\frac{2z}{D}\right)^{2.2}\right\} \times \left\{1 - \left(\frac{2x}{D}\right)^{2.2}\right\} \tag{2}$$

where the origin $x = z = 0$ coincides with the centre of the square cross-section. The main channel is 7D long whereas the branched channel is 3D long. The objective is to predict the fraction of inflow exiting through the main channel for three angles Ψ between the two channels. The exit pressure in both branches is fixed at $p_{ex} = 1$. Computations are performed with $\Psi = 90$ (3390 elements), 60 (3581 elements) and 30 (3609 elements) and employing UDS ($\beta = 0$). The tetrahedral elements are generated using ANSYS. Table 2 presents values of FFR and C_p defined as

$$\text{FFR} = \frac{\text{Exit Mass Flow through Main Branch}}{\text{Mass Flow at Inlet}}$$
$$C_p = \frac{p_{in} - p_{ex}}{\rho u_{in}^2} \tag{3}$$

where p_{in} and u_{in} are average pressure and velocity at inflow plane. The table shows that irrespective of the angle, the flow-fraction in the main branch increases with Reynolds number whereas the pressure-coefficient decreases. Similarly, for a given *Re*, the flow fractions through the main branch decrease with decrease in the angle but, C_p values show non-monotonous trend. At high *Re*, the C_p values are negative indicating that the average pressure at the inlet plane is less than exit pressure. To our knowledge, there are no experimental or numerical data available for comparison.

Table 2
FFR and C_p for 3D branch

Re	$\Psi = 90$		$\Psi = 60$		$\Psi = 30$	
	FFR	C_p	FFR	C_p	FFR	C_p
20	0.5289	7.974	0.5176	8.270	0.4675	8.154
100	0.6167	1.5692	0.5794	1.659	0.4975	1.565
200	0.6683	0.6458	0.621	0.6810	0.5221	0.5757
300	0.7028	0.3107	0.6528	0.320	0.5382	0.2124
400	0.7276	0.1336	0.6807	0.1335	0.5432	0.011
500	0.7450	0.0204	0.7046	0.0205	0.5459	−0.1166
600	0.7623	−0.050	0.7244	−0.0463	0.526	−0.192

2.5. Tube containing a twisted tape

Consider flow in a tube containing a twisted tape of thickness δ. The width of the tape equals tube internal diameter *D* as shown in Fig. 8. The axial distance for 180° rotation of the tape equals *H*. The flow is *fully-developed* and laminar. The heat transfer is under axially and peripherally constant wall flux (q_w) condition but the tape contributes negligibly to finning. Under these conditions, the Fanning friction factor *f* and Nusselt number *Nu* are governed by [14]

$$f\,Re = F(Re, Y)$$
$$Nu = \frac{hD}{k} = \frac{q_w}{(\overline{T}_w - T_b)}\frac{D}{k} = F(Re, Y, Pr) \tag{4}$$

where $Re = \bar{u}_3 D/\nu$, $\overline{T}_w$ is *circumferentially* averaged tube wall temperature, T_b is fluid bulk temperature and, the tape-twist parameter *Y* is defined as

$$Y = \frac{H}{D} \tag{5}$$

In a fixed coordinate system (x, y, z), the flow is three-dimensional. However, by defining a *rotating* coordinate system $(x_1, x_2, x_3 = z)$ that rotates with the orientation of

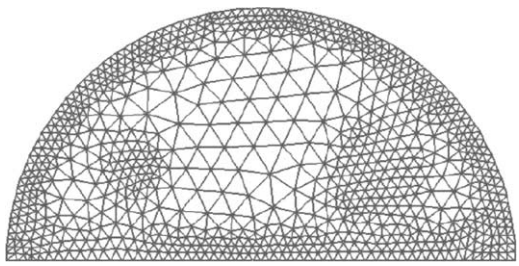

Fig. 9. Unstructured mesh—twisted tape problem.

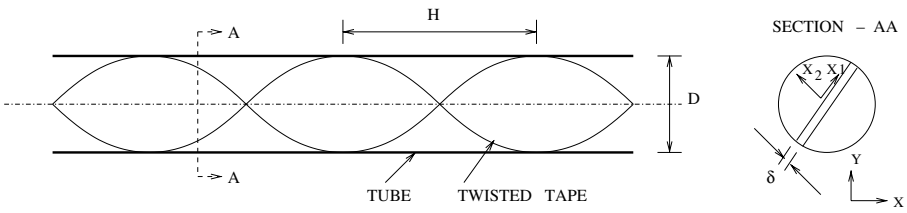

Fig. 8. Tube containing a twisted tape.

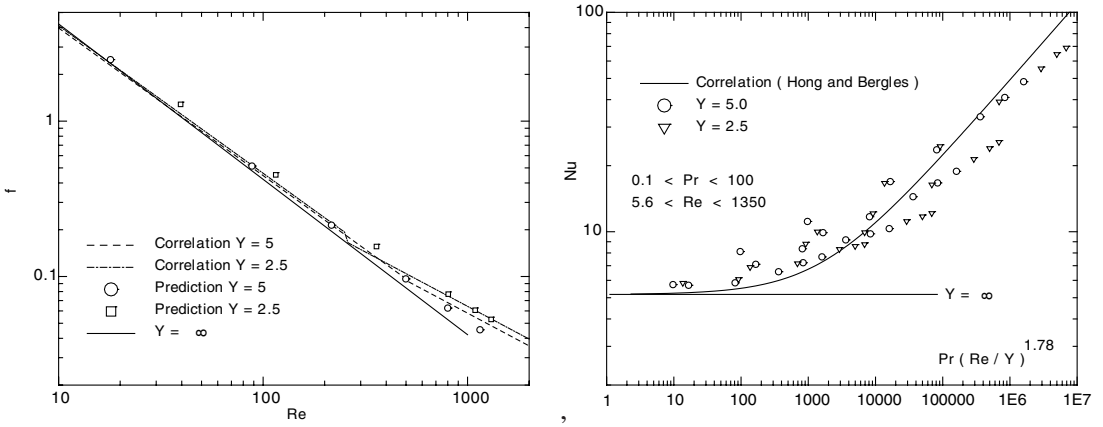

Fig. 10. Friction factor and Nusselt number—twisted tape problem.

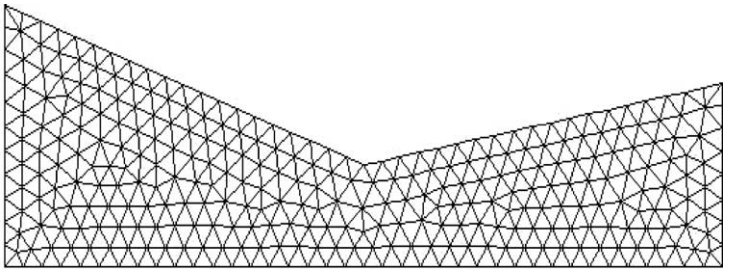

Fig. 11. Triangular mesh—2D plane nozzle.

the tape, the governing equations can be rendered two-dimensional under fully developed conditions because $\partial\Phi/\partial x_3 = 0$ for all variables except pressure and temperature. The mean pressure gradient $\partial\bar{p}/\partial x_3 = \text{constant}$. Similarly, $\partial T/\partial x_3 = \partial T_b/\partial x_3 = \text{constant}$ and the value of the constant is derived from energy balance. The transport equation must therefore be transformed into rotating coordinate system. The resulting equations are given in [15] and, therefore, not repeated here. The equations for $\Phi = u_1, u_2, u_3, p'$ and T are solved in a semicircular domain assuming flow symmetry about the tape of zero thickness ($\delta = 0$) because in practical applications $\delta/D \sim 1/30$. Computations are performed for a prescribed axial pressure gradient $\partial\bar{p}/\partial x_3$. The mean velocity $\bar{u}_3$ and, hence, Re is the solution. Fig. 9 shows the unstructured mesh (1594 elements and 873 vertices). Cell-density in near-wall regions is increased to accurately capture high temperature gradients at high Prandtl numbers. The predicted friction factor data are compared in Fig. 10 with the following correlation due to Date and Singham [14]:

$$\begin{aligned} f &= \frac{38.4}{Y^{0.05}\,Re^{0.95}} \quad \text{for } \frac{Re}{Y} < 100 \\ f &= C\left(\frac{Re}{Y}\right)^{-0.7} \quad \text{for } \frac{Re}{Y} > 100 \end{aligned} \tag{6}$$

where $C = 8.8201 - 2.1193\,Y + 0.2108\,Y^2 - 0.0069\,Y^3$. The correlation is based on numerical predictions but has been found to predict experimental data of Saha et al. [12] within ±13%. Note that for $Y = \infty$ (that is, untwisted tape), an exact solution due to Weigand [20] predicts $fRe = 42.23$. The predicted data for finite Y show that irrespective of twist, at low Reynolds numbers, the fRe values do indeed asymptotically approach 42.23 as expected. Fig. 10 also shows comparison of the presently computed Nu-data [2] for $0.1 < Pr < 100$ with the following experimental correlation due to [13].

$$Nu = 5.172\left[1 + 0.005484\,Pr^{0.7}\left(\frac{Re}{Y}\right)^{1.25}\right]^{0.5} \tag{7}$$

The correlation predicts experimental data of [13] within ±25%. Similar agreement is found for 90% of the presently computed data. The value $Nu = 5.172$ corresponds to $Y = \infty$. Again, the present data asymptotically approach this value at low Reynolds numbers.

[2] Note that the Nu-data are plotted against $Pr(Re/Y)^{1.78}$ as recommended by Hong and Bergles [13].

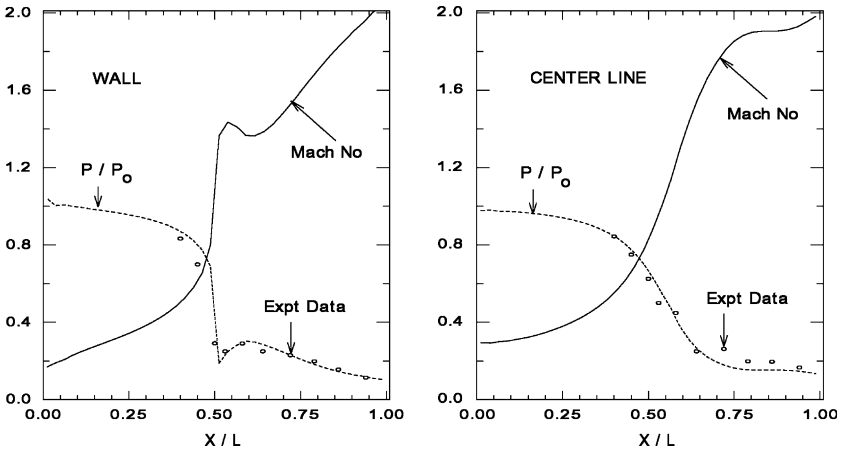

Fig. 12. Variation of pressure and Mach number.

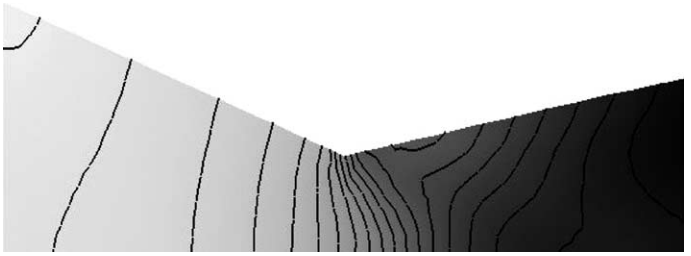

Fig. 13. Mach number contours.

2.6. Plane convergent–divergent nozzle

Consider a 2D plane convergent–divergent nozzle shown in Fig. 11. The total length of the nozzle is 11.56 cm and throat is midway. The inlet, throat and exit sections are respectively 3.52, 1.37 and 2.46 cms high when measured from the symmetry axis. The inlet Mach no is $M_{in} = 0.232$ and exit static pressure is fixed at $P_{ex}/P_{stag} = 0.1135$. Computations are performed by generating a triangular mesh (570 elements). The flow is taken to be *inviscid*, that is, $\mu = 0$ and stagnation enthalpy is assumed constant.

The novel feature of this compressible flow computation is the use of TVD scheme due to [18] for representation of convective transport (see Part I [1]). At inflow plane, since M_{in} is known, u_{in}, T_{in} and p_{in} are specified using standard isentropic relations. At exit plane, except for pressure (which is fixed), all other variables are linearly extrapolated from near-boundary values. At the upper wall, *tangency* condition is applied. The pressure distribution is determined by solving the compressible flow version of the total pressure-correction equation. Momentum equations for $\Psi = u_1, u_2$ are solved and temperature is determined from assumed stagnation enthalpy. Finally, density is determined from equation of state $p = \rho RT$.

The computed results for p/p_{stag} (dotted line) and M (solid line) are plotted in Fig. 12. The experimental data for p/p_{stag} (open circles) are due to Mason et al. [19]. The figure shows good agreement with the experimental data. Note also that wall Mach number passes sharply through $M = 1$ exactly at the throat ($X/L = 0.5$) and reaches $M = 2.01$ at exit. At the centerline, the $M = 1$ location is downstream of throat. The iso-Mach number contours are slanted (see Fig. 13).

3. Conclusions

(1) The calculation procedure described in [1] has been successfully applied to several problems with different geometric complexities, presence of body and surface forces and boundary conditions.

(2) The procedure is able to predict accurate results using relatively coarse grids. The blended convection scheme is found useful for reducing false numerical diffusion.

References

[1] A.W. Date, Solution of transport equations on unstructured meshes with cell-centered colocated variables. Part I. Discretization, Companion Paper, this volume.

[2] B.N. Jiang, T.L. Lin, L.A. Povinelli, Large-scale computation of incompressible viscous flow by least-squares finite element method, Comput. Meth. Appl. Mech. Eng. 119 (1994) 109.

[3] Y. Zhao, B. Zhang, A high-order characteristic upwind FV method for incompressible flow and heat transfer simulation on unstructured grid, Comput. Meth. Appl. Mech. Eng. 190 (2000) 733.

[4] W.H. Leong, K.G. Hollands, A.P. Brunger, On a physically realizable benchmark problem in the internal natural convection, Int. J. Heat Mass Transfer 41 (1998) 3817–3828.

[5] W.H. Leong, K.G. Hollands, A.P. Brunger, Experimental Nusselt numbers for a cubical-cavity benchmark problem in natural convection, Int. J. Heat Mass Transfer 42 (1999) 1979–1989.

[6] D.W. Pepper, K.G.T. Hollands, Benchmark summary of numerical studies: 3-D natural convection in an air-filled enclosure, in: ICHMT 2nd Int. Symp. on Adv. in Comp. Heat Transfer, Palm Cove, Australia, 2001, p. 1323.

[7] F.L. Bennecer, A.A. Mohammed, I. Sezai, Transient natural convection in air-filled cubical cavity—validation exercise, in: ICHMT 2nd Int. Symp. on Adv. in Comp. Heat Transfer, Palm Cove, Australia, 2001, p. 1383.

[8] R. Mossad, Prediction of natural convection in an air-filled cubical cavity using FLUENT Software, in: ICHMT 2nd Int. Symp. on Adv. in Comp. Heat Transfer, Palm Cove, Australia, 2001, p. 1371.

[9] E. Krepper, CHT01 validation exercise: natural convection in an air-filled cubical cavity, in: ICHMT 2nd Int. Symp. on Adv. in Comp. Heat Transfer, Palm Cove, Australia, 2001, p. 1351.

[10] C. Xia, J.Y. Murthy, S.R. Mathur, Finite-volume computations of buoyancy-driven flow in a cubical cavity: a benchmarkinf exercise, in: ICHMT 2nd Int. Symp. on Adv. in Comp. Heat Transfer, Palm Cove, Australia, 2001, p. 1345.

[11] S.R. Mathur, J.Y. Murthy, A pressure-based method for unstructured meshes, Numer. Heat Transfer, Part B 31 (1997) 195–215.

[12] S.K. Saha, U.N. Gaitonde, A.W. Date, Heat transfer and pressure-drop characteristics of laminar flow in a tube fitted with regularly spaced twisted tape elements, J. Exp. Thermal Fluid Sci. 2 (1989) 310–322.

[13] S.W. Hong, A.E. Bergles, Augmentation of laminar flow and heat transfer by means of twisted tape inserts, J. Heat Transfer 98 (1976) 251–256.

[14] A.W. Date, J.R. Singham, Numerical prediction of friction and heat transfer characteristics of fully-developed laminar flow in tubes containing twisted tapes, AIChE-ASME Heat Transfer Conference, Denver, USA, Paper No. 72-HT-17, 1972.

[15] A.W. Date, Numerical prediction of laminar flow and heat transfer in a tube with twisted tape insert: effects of property variations and buoyancy, Enhanced Heat Transfer 7 (2000) 217–229.

[16] H. Choi, D. Lee, J.S. Maeng, A node-centred pressure-based method for all speeds on unstructured meshes, Numer. Heat Transfer, Part B 44 (2003) 165–185.

[17] R.E. Hayes, K. Nandkumar, H. nasr-El-din, Laminar flow in a 90 degree planar branch, Comput. Fluids 17 (1989) 537–553.

[18] C.H. Lin, C.A. Lin, Simple high-order bounded convection scheme to model discontinuities, AIAA J. (35) (1997) 563–565.

[19] M.L. Mason, L.E. Putnam, R.J. Re, The effect of throat contouring on two-dimensional converging-diverging nozzle at static conditions, NASA Tech Paper 1704, 1980.

[20] A. Weigand, The problem of torsion in prismatic members of circular segmental cross section, NACA TM-1182, 1944.

[21] N.M. Natarajan, S.M. Laksmanan, Laminar flow in rectangular ducts: prediction of velocity profiles and friction factor, Indian J. Technol. 10 (1972) 435–438.